NEUROSCIENCE

A distributed circuit for associating environmental context with motor choice in retrosplenial cortex

Luis M. Franco[1] and Michael J. Goard[1,2,3]*

During navigation, animals often use recognition of familiar environmental contexts to guide motor action selection. The retrosplenial cortex (RSC) receives inputs from both visual cortex and subcortical regions required for spatial memory and projects to motor planning regions. However, it is not known whether RSC is important for associating familiar environmental contexts with specific motor actions. We test this possibility by developing a task in which motor trajectories are chosen based on the context. We find that mice exhibit differential predecision activity in RSC and that optogenetic suppression of RSC activity impairs task performance. Individual RSC neurons encode a range of task variables, often multiplexed with distinct temporal profiles. However, the responses are spatiotemporally organized, with task variables represented along a posterior-to-anterior gradient along RSC during the behavioral performance, consistent with histological characterization. These results reveal an anatomically organized retrosplenial cortical circuit for associating environmental contexts with appropriate motor outputs.

INTRODUCTION

The ability to navigate through familiar locations is a fundamental cognitive capability underlying a wide range of animal behaviors, including foraging, nesting, and escape from predation. A wealth of research has focused on navigational strategies that require a "cognitive map" of the local environment (*1*, *2*). However, in familiar environments, animals often use route-following strategies that involve recognizing learned environmental contexts and using them to guide motor action. For instance, when traveling between two familiar locations (e.g., home and work), we do not need to rely on a cognitive map but can instead recognize familiar visual scenes (e.g., particular intersections) and use them to guide our actions. Although this ability seems simple, it requires neuronal integration of diverse streams of sensory cues and learned associations to select appropriate motor actions. Despite the importance of this ability for animal behavior, the neural circuitry linking the association of the current environmental context to motor selection is poorly understood.

Subcortical regions such as the hippocampal formation are known to be important for spatial navigation. However, it has become increasingly clear that neocortical regions also play a crucial role in navigation, in particular for remote spatial memories (*3*–*7*). Although patients with hippocampal lesions have difficulty learning to navigate novel environments, they retain the ability to navigate through locations that were familiar before the lesion (*8*). In this regard, the retrosplenial cortex (RSC) has attracted particular attention because of its anatomical connectivity with visual cortex (VC), parietal cortex (PPC), premotor cortex, anterior thalamic nuclei, and the hippocampal formation (*3*, *5*). Damage to RSC in humans results in navigation deficits even in familiar locations (*5*, *9*). Similar results have been found in rodents, although the effect appears to vary with the extent of the RSC lesion (*10*–*14*). These studies indicate a role for RSC in the storage and recognition of familiar locations during navigation.

Previous studies have shown that subsets of RSC neurons are tuned to allocentric and egocentric spatial variables, including position (*15*–*17*), head direction (*18*–*20*), proximity to landmarks (*21*–*25*), and proximity to boundaries (*26*, *27*). However, RSC neurons are also important for the memory of environmental "contexts," defined as general locations that are identifiable by invariant sensory features and that are independent of the current position or trajectory (e.g., a specific intersection, regardless of which lane one is in). Specifically, exposure to new environmental contexts increases immediate early gene expression in RSC (*28*–*30*), and disruption of RSC can impair the recall of specific contexts (*31*, *32*). In addition, conditioned freezing responses to a particular environmental context can be artificially evoked via optogenetic stimulation of subsets of RSC neurons that exhibited elevated c-Fos expression during exposure to the context (*33*, *34*). Together, these results suggest a role for RSC in remote memory of environmental contexts independent of egocentric or allocentric spatial variables (*5*).

To investigate whether RSC plays a role in associating familiar environmental contexts with motor choice independent of local spatial variables, we developed a virtual T-maze task for head-fixed mice in which the wall pattern determined which turn direction would be rewarded. To dissociate the environmental context from other spatial cues (such as position, orientation, and proximity of boundaries), we decoupled mouse position in the environment from physical locomotion, limiting mice to a binary choice of maze trajectory, which was selected using a rotary joystick. It should be noted that this task design lacks the somatosensory, proprioceptive, and vestibular input that would be present during movement through a physical environment. In this sense, the task more closely resembles navigation performed by humans in vehicles or virtual environments. To avoid confusion, we describe this as an association task (specifically, the association of environmental context with a motor action) rather than a navigation task. That said, understanding the association between environmental context and motor selection has clear implications for navigation, in particular during route-following.

Once mice were trained to expert levels on the task, we used widefield calcium imaging of the dorsal cortical surface to screen for regions showing differential activity during association of environmental context with motor planning. Widefield calcium activity

[1]Neuroscience Research Institute, University of California, Santa Barbara, CA 93106, USA. [2]Department of Molecular, Cellular, and Developmental Biology, University of California, Santa Barbara, CA 93106, USA. [3]Department of Psychological and Brain Sciences, University of California, Santa Barbara, CA 93106, USA.
*Corresponding author. Email: michael.goard@lifesci.ucsb.edu

revealed higher RSC activity before decision on correct trials relative to incorrect trials. Photoinhibition of RSC excitatory neurons during the predecision period led to impaired performance on the task, indicating that RSC activity plays an important role in the association of environmental contexts with appropriate motor choice. Two-photon imaging of populations of RSC neurons indicated that individual neurons encode sensory context, motor choice, and trial outcome variables, with a subset of neurons jointly encoding multiple variables with distinct temporal dynamics. Last, we found anatomical gradients in the encoding of particular task variables, with posterior RSC encoding environmental context and choice bias signals, while motor planning, motor execution, and trial outcome were encoded throughout the extent of RSC. This functional organization is consistent with anatomical connectivity from visual cortex to posterior RSC and from anterior RSC to forelimb motor area, respectively. Together, these results reveal a circuit spanning posterior-to-anterior RSC for associating environmental contexts with appropriate motor planning signals, even in the absence of physical locomotion.

RESULTS

A task for association of environmental context with trajectory in the absence of locomotion

To investigate neural activity during the association of environmental context with motor action, we developed a virtual T-maze task in which head-fixed mice use a rotary joystick to select one of two trajectories based on visual cues (Fig. 1A, movie S1, and fig. S1; see Materials and Methods), allowing us to quantify task variables independently of locomotion and local spatial variables. The contexts varied with respect to pattern (context 1, dashed; context 2, striped), orientation (context 1, 90° from vertical; context 2, 45° from vertical), and color (context 1, yellow; context 2, blue). Each context was associated with a particular rewarded arm (context 1, left; context 2, right; Fig. 1B). Note that the contexts were symmetrical on both sides of the maze, so mice had to recall associations with abstract visual patterns rather than simply orienting to a stimulus appearing on one side. At the start of each trial, the joystick was locked to the center position, and the mouse was presented with one of the two contexts. The mouse then progressed automatically at a fixed speed through the stem of the virtual T-maze (3-s duration) until stopping at a decision point shortly before the split in the T-maze. At this point, the joystick was unlocked, and mice were given a 3-s window to rotate the joystick left or right to a set angular threshold to indicate their decision. During the decision window, the joystick movements were locked to rotation of the virtual environment in a closed loop. If the mouse made a decision within the window, the joystick was locked and a sound indicating the trial outcome was played. The mouse then proceeded automatically to the end of the selected T-maze arm (3-s duration), which contained a visual cue indicating reward for correct decisions or no cue for incorrect decisions. Last, there was a fixed 3-s intertrial interval before mice were teleported back to the beginning of the T-maze for the start of the next trial.

After 46 to 50 training sessions, mice ($n = 18$) increased the number of responses up to an average of 81.1 ± 2.9 decisions per session with a mean performance rate of 82.5 ± 0.8% (Fig. 1, C to F, and fig. S2, A and B). Learning was accompanied by a decrease in response latency (fig. S2, C and D) and a selective increase in correct decisions (fig. S2, E and F). We observed no consistent bias in left versus right responses throughout training (fig. S2G). Performance was

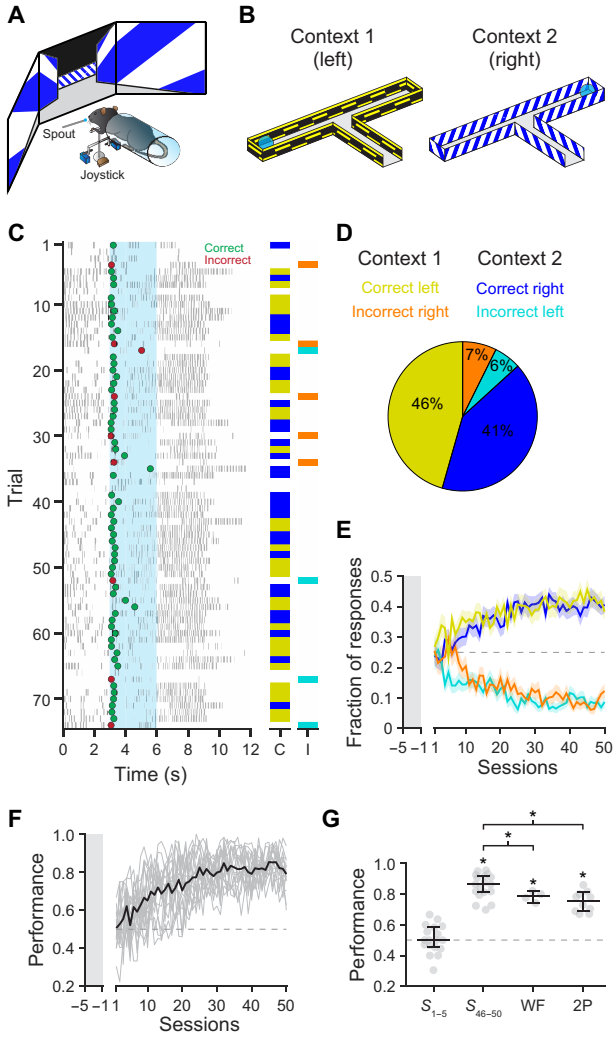

Fig. 1. A task for association of context with trajectory in the absence of locomotion. (**A**) Schematic of behavioral setup. Mice use a rotary joystick to choose trajectories in a virtual T-maze presented on monitors spanning the horizontal visual field. (**B**) Schematic of the T-maze task for head-fixed mice in the absence of locomotion. Left turns are rewarded in context 1, whereas right turns are rewarded in context 2. (**C**) Example behavioral session. Dots indicate decisions (green = correct and red = incorrect); gray tick marks indicate licking; cyan shading indicates the decision window. Columns on the right show correct (C; yellow/blue) and incorrect (I; orange/cyan) responses in the two contexts. Trials in which no choice was made within the decision window are left blank. (**D**) Summary of the behavioral responses for the session shown in C (yellow = correct left, orange = incorrect right, blue = correct right, and cyan = incorrect left). (**E**) Fraction of response types during behavioral training ($n = 18$ mice). Mice are habituated to the training rig for 5 days (gray shaded area), during which the joystick can only rotate the correct direction to establish context-reward associations. Following habituation, the fraction of free decisions is progressively increased (10 to 80% of trials); only free decision trials are analyzed. Lines indicate mean ± SEM; colors as in (D). (**F**) Performance during behavioral training ($n = 18$ mice). Performance of individual mice is shown in gray. Average performance is shown in black. (**G**) Plots displaying performance during the first 5 days of training (S_{1-5}), last 5 days of training (S_{46-50}), widefield imaging sessions (WF), and two-photon imaging sessions (2P). Mouse performance was significantly above chance during late training and imaging sessions [$S_{1-5} = 50.0\%$; $S_{46-50} = 86.4\%$; WF = 78.9%; 2P = 75.5%; asterisks indicate lower 95% confidence interval (CI) > 50%]. Gray dots, individual mice; Black overlay, median ± 95% CI.

significantly above chance for all analyzed physiology sessions, although there was a small decrease in performance between expert training sessions (86.4%) and both widefield imaging sessions (78.9%, $P = 0.03$, Wilcoxon rank sum) and two-photon imaging sessions (75.5%, $P = 0.0001$, Wilcoxon rank-sum; Fig. 1G). To determine whether mice waited until the decision point before planning their response, we transferred a subset of fully trained mice to a closed-loop version of the task in which forward movement progressed automatically, but angular rotation was controlled in a closed-loop fashion throughout the T-maze. We found that mice performed significantly above chance (72.4 ± 1.4%) and began turning toward the chosen direction well before the decision point (fig. S2, H to K), indicating that choice planning was initiated before the decision window. Note that mice with full control of their trajectory would have exhibited different head direction, proximity to boundaries, and visual input across trial types, conflating the environmental context with other sensory and spatial variables.

Dysgranular RSC plays an important role in accurate context-to-trajectory associations

As a first step toward examining cortical responses during the association task, we imaged the dorsal cortex in transgenic mice with pan-excitatory expression of GCaMP6s ($n = 20$ imaging sessions in four mice; Fig. 2A; see Materials and Methods). For these mice, the skull was polished and overlaid with a coverslip to allow imaging of an 8- to 10-mm-diameter region, including VC, RSC, PPC, somatosensory (SSC), and somatomotor cortices (SMC) (Fig. 2, B and C). During all trial types, activity was highest in VC and RSC before the decision (0 to 3 s; Fig. 2D). Following the joystick movement (3 to 6 s; Fig. 2D), activity was highest in the SMC and anterior SSC, centered over the caudal forelimb area (CFA), which is necessary for planning and executing forelimb movements (*35*, *36*). To determine whether particular cortical regions exhibited differential activity during successful context-to-trajectory associations, we measured the subtracted response (correct trials – incorrect trials), revealing a small but significant increase in activity in RSC but not in other regions during the predecision period [$RSC_{-1.5–0s} = 0.26 \pm 0.19\ \Delta F/F$, $P = 0.021$ (not significant); $RSC_{0–1.5s} = 0.36 \pm 0.19\ \Delta F/F$, $P = 0.0046$; and $RSC_{1.5–3s} = 0.39 \pm 0.19\ \Delta F/F$, $P = 0.0035$; Wilcoxon sign-rank test with Bonferroni correction; Fig. 2, E and G, and fig. S3, A and B]. After the decision point, activity was higher in several regions on correct trials, most noticeably, the CFA (*36*), spanning anatomically defined SSC and SMC regions ($SMC_{3–4.5s} = 2.36 \pm 0.21\ \Delta F/F$, $P = 8.8 \times 10^{-8}$; $SSC_{3–4.5s} = 2.73 \pm 0.21\ \Delta F/F$, $P = 3.6 \times 10^{-8}$; $SMC_{4.5–6s} = 0.71 \pm 0.17\ \Delta F/F$, $P = 3.0 \times 10^{-4}$; and $SSC_{4.5–6s} = 0.83 \pm 0.15\ \Delta F/F$, $P = 2.9 \times 10^{-5}$; Wilcoxon sign-rank test with Bonferroni correction; Fig. 2, F and G). Moreover, space-frequency singular value decomposition analysis (*37*) revealed notable differences in the initiation and spatiotemporal progression of neural activity between correct and incorrect trials (fig. S3C). To maximize temporal resolution, we did not perform hemodynamic correction of widefield images during behavior. We found that while the calcium responses measured with the GCaMP6s indicator are much larger than the hemodynamic responses (*38*), there is some residual hemodynamic contamination of the calcium responses (fig. S4). It should also be noted that lack of differential widefield activity on correct and incorrect trials does not rule out a role for other dorsal cortical regions, as there might be more subtle changes in activity patterns that are not evident using widefield imaging.

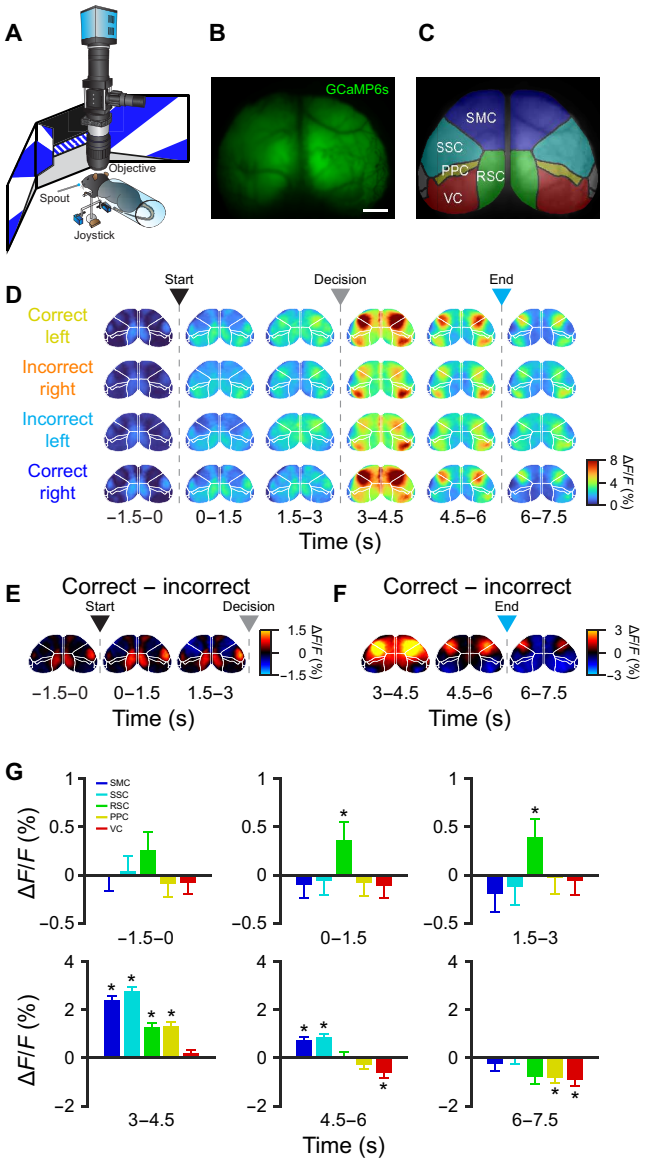

Fig. 2. Differential mesoscale activity in RSC during context-trajectory associations. (**A**) Schematic of widefield imaging of calcium activity across dorsal cortex during task performance. (**B**) The skull of transgenic mice expressing GCaMP6s was polished and overlaid with cyanoacrylate and a coverslip to allow imaging of an 8- to 10-mm-diameter region of dorsal cortex. Scale bar, 1 mm. (**C**) Regions of dorsal cortex imaged during performance of the task. Region parcellation based on the Allen Mouse Brain Common Coordinate Framework (*80*). (**D**) Average registered activity maps obtained in 1.5-s epochs during traversal of the T-maze for all trial types ($n = 20$ sessions in four mice). Arrowheads and dashed lines indicate trial start (black), decision point (gray), and trial end (cyan). (**E** and **F**) Maps obtained by subtracting correct trials minus incorrect trials. Note that activity is higher in RSC in correct trials before the decision point (pooled across both contexts). After decisions, activity is higher in SMC in correct trials. Arrowheads and dashed lines indicate trial start (black), decision point (gray), and trial end (cyan). (**G**) Bar plots indicating significantly higher RSC activity in correct trials before the decision point. After decisions, SMC and SSC exhibit higher activity (3 to 6 s), whereas RSC and PPC have both higher (3 to 4.5 s) and lower (RSC, 6 to 7.5 s; PPC, 4.5 to 7.5 s) activity in correct trials. VC activity, by contrast, is lower by the end of correct trials (4.5 to 7.5 s). All values are means ± SEM, asterisks indicated statistical significance, *$P < 0.01$; Wilcoxon sign-rank test with Bonferroni correction ($\alpha = 0.01$).

To test whether RSC activity is necessary for performance of the association task, we virally expressed the inhibitory opsin ArchT along the anterior-posterior extent of RSC in both hemispheres (Fig. 3, A and B). Recent reports have suggested that direct photoinhibition can reduce off-target effects compared to indirect photoinhibition via stimulation of inhibitory neurons (*39*). We found that ArchT-mediated suppression was power dependent and resulted in no detectable off-target suppression of cortical activity outside of RSC ($ArchT_{0.5mW}$ = −0.3 ± 0.2 Δ*F*/*F* and $control_{0.5mW}$ = 0.1 ± 0.3 Δ*F*/*F*, *P* = 0.2145; $ArchT_{10mW}$ = −2.8 ± 0.1 Δ*F*/*F* and $control_{10mW}$ = 1.1 ± 0.2 Δ*F*/*F*, $P = 3.7 \times 10^{-5}$; $ArchT_{20mW}$ = −4.7 ± 0.2 Δ*F*/*F* and $control_{20mW}$ = 0.6 ± 0.1 Δ*F*/*F*, $P = 3.7 \times 10^{-5}$; $ArchT_{30mW}$ = −6.3 ± 0.2 Δ*F*/*F* and $control_{30mW}$ = −0.3 ± 0.2 Δ*F*/*F*, $P = 3.7 \times 10^{-5}$; $ArchT_{40mW}$ = −7.7 ± 0.2 Δ*F*/*F* and $control_{40mW}$ = −0.8 ± 0.2 Δ*F*/*F*, $P = 3.7 \times 10^{-5}$; and $ArchT_{50mW}$ = −8.4 ± 0.2 Δ*F*/*F* and $control_{50mW}$ = −0.7 ± 0.1 Δ*F*/*F*, $P = 3.7 \times 10^{-5}$; Wilcoxon sign-rank test; mean ± SEM; *n* = 12 sessions in four mice; Fig. 3, C and D). However, we cannot rule out off-target suppression of interconnected subcortical regions such as the anterior thalamic nuclei (*40*). During randomly interleaved light exposure trials, we found that RSC inhibition resulted in a substantial impairment in task performance [$ArchT^{+}_{off}$ = 80.6 ± 6.3% and $ArchT^{+}_{on}$ = 42.2 ± 9.5%; linear mixed-effects model, fixed effect for condition, and random effect for mouse and session; condition effect: $t(22) = -8.87$, $P < 0.0001$; *n* = 12 sessions in four mice; Fig. 3E]. This impairment was not seen in mice expressing GCaMP6s alone with the same illumination protocol [$ArchT^{-}_{off}$ = 78.3 ± 10.2% and $ArchT^{-}_{on}$ = 79.6 ± 14.3%; linear mixed-effects model, fixed effect for condition, and random effect for mouse and session; condition effect: $t(10) = 0.17$, $P = 0.87$; $n = 6$ sessions in two mice; Fig. 3E], ensuring that the effect is not due to nonspecific effects on tissue temperature (*41*). Optogenetic stimulation did not affect the response fraction ($ArchT^{+}_{off}$ = 70.7 ± 10.5% and $ArchT^{+}_{on}$ = 78.3 ± 11.3%, *P* = 0.9966; Wilcoxon sign-rank test; *n* = 12 sessions in four mice; Fig. 3F) but rather decreased the proportion of correct to incorrect decisions [$ArchT^{+}_{CL}$ = 38.9 ± 5.4% and $ArchT^{+}_{IR}$ = 9.7 ± 7.2%, trial type effect: $t(22) = 4.84$, $P < 0.0001$; $ArchT^{+}_{IL}$ = 9.7 ± 6.3% and $ArchT^{+}_{CR}$ = 41.7 ± 8.0%, trial type effect: $t(22) = 7.67$, $P < 0.0001$; mean ± SD; Fig. 3G] and light on trials [$ArchT^{+}_{CL}$ = 21.5 ± 7.3% and $ArchT^{+}_{IR}$ = 28.8 ± 9.2%, trial type effect: $t(22) = -1.09$, $P = 0.29$; $ArchT^{+}_{IL}$ = 29.0 ± 10.5% and $ArchT^{+}_{CR}$ = 20.7 ± 11.0%, trial type effect: $t(22) = -1.03$, $P = 0.32$; linear mixed-effects model with fixed effect for trial type and random effect for mouse and session; *n* = 12 sessions in four mice]. Together, these results indicate that RSC plays an important role during context-to-trajectory associations, even when the mouse is not required to physically navigate through space.

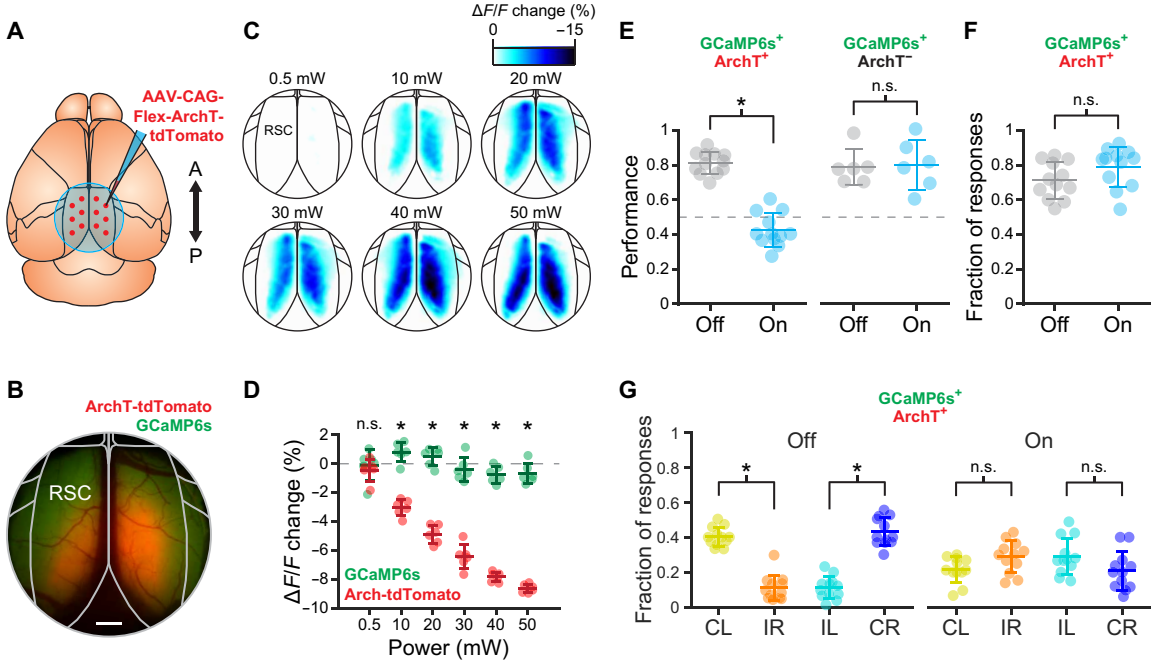

Fig. 3. Suppression of RSC activity impairs context-trajectory associations. (**A**) Transgenic mice expressing GCaMP6s were injected with AAV-CAG-Flex-ArchT-tdTomato (red dots: approximate injection sites) along the rostrocaudal extent of RSC in both hemispheres to drive expression of the inhibitory opsin ArchT. (**B**) Example mouse showing expression of ArchT (red) and GCaMP6s (green). Scale bar, 500 μm. (**C**) Activity maps showing the suppression of spontaneous activity in RSC immediately following (1-s window) randomly presented light pulses (550 nm, 0.5 to 50 mW) compared to immediately before the pulse (1-s window) in an example ArchT-expressing mouse at different power intensities. (**D**) Change in RSC spontaneous activity in the region exhibiting expression of ArchT (red) and in a control region outside of RSC only exhibiting expression of GCaMP6s [green; see (B)]. Increasing light-emitting diode (LED) power progressively decreased activity in RSC (mean ± SEM; *n* = 12 sessions in four mice; asterisks indicate statistical significance, Wilcoxon sign-rank test). (**E**) Behavioral performance of $ArchT^{+}$ mice (left) was impaired in randomly interleaved trials (25%) by optogenetic inhibition of RSC activity during initial traversal of the stem of the T-maze and the decision window (*n* = 12 sessions in four mice). Asterisks indicate significant effect of condition in linear mixed-effects model. No effect was seen in $ArchT^{-}$ mice (right; *n* = 6 sessions in two mice). Lines indicate mean ± SD. n.s., not significant. (**F**) No change in the fraction of behavioral responses between trials with and without optogenetic stimulation in $ArchT^{+}$ mice (Wilcoxon sign-rank test; mean ± SD). (**G**) Fraction of correct and incorrect responses for both contexts in $ArchT^{+}$ mice during light off trials and light on trials. Asterisks indicate significant effect of condition in linear mixed-effects model, **P* < 0.001. Lines indicate mean ± SD.

Single neurons in RSC encode context, motor, and outcome task variables

To determine how individual RSC excitatory neurons encode task variables, we used two-photon microscopy to measure calcium responses from 7770 Layer 2/3 neurons (29 planes from 10 mice; all planes located 90 to 155 μm below pia) in bilateral RSC (Fig. 4, A to C, and fig. S5; see Materials and Methods). A majority (5194 of 7770 neurons, 66.8%) of the individual neurons exhibited significant reliable responses across one of the two correct trial types (see Materials and Methods), with a subset (2818 neurons, 54.3%) responding to a single correct trial type and the rest (2376 neurons, 45.7%) responding to both correct trial types, although often with different temporal dynamics (Fig. 4D; additional example neurons in fig. S6). Aligning the population of responses across experiments to trial time (decision window excluded; see Materials and Methods) revealed that roughly equal numbers of neurons preferred each correct trial type (Fig. 4E). As previously observed, RSC neurons exhibited broad but reliable responses (*23*), with peak responses spanning the entire trial duration (Fig. 4, E and F). However, particular epochs of the trial, including the trial start, decision point, and trial end exhibited higher numbers of responsive neurons (Fig. 4G). Moreover, the response magnitude of the responsive neurons tended to be larger in the later epochs of the trial (Fig. 4H).

To visualize the population activity in a lower-dimensional space corresponding to task variables, we performed targeted dimensionality reduction (*42*), revealing that different task variables show distinct encoding dynamics in the population throughout the trial (Fig. 4, I and J, and fig. S7). To further investigate encoding of task variables in individual neurons and populations (*43*–*46*), we used a linear support vector machine classifier (*47*, *48*) to measure encoding of context (context 1/context 2), motor output (left/right), and outcome (rewarded/unrewarded) in 100-ms bins spanning the trial (see Materials and Methods). A subset of individual neurons encoded single task variables at above-chance levels, although rarely at ceiling levels due to high intertrial variability (Fig. 5, A and B, cells 1 to 3; and fig. S8, cells 5 to 10). Many individual neurons exhibited multiplexed encoding of multiple task variables with distinct time courses (Fig. 5, A and B, cell 4; and fig. S8, cells 11 and 12). The population of RSC neurons was able to decode context, motor output, and outcome at high-performance levels, although with distinct time courses (Fig. 5C). Soon after visual cue onset, decoding performance of the context increased and remained high until the offset of visual cues at the end of the trial [Fig. 5, C (top) to E]. Unexpectedly, motor output could be decoded at above-chance levels (62.9 ± 6.0%) before visual cue onset, indicating the presence of a motor output bias before the start of the trial [Fig. 5, C (middle) to E]. Motor output encoding performance continued to increase during the approach corridor and peaked shortly after the decision, remaining at high levels throughout the rest of the trial [Fig. 5, C (middle) to E]. Last, outcome encoding performance was at chance until after the decision, exhibited a peak during the sound indicating the response outcome, and then rose sharply toward the end of the trial [Fig. 5, C (bottom) to E]. Note that encoding of motor or outcome variables after the decision point may be due to efferent copy feedback resulting from limb movement or licking (*49*, *50*).

It has recently been shown that trial history is encoded in association cortex (*51*, *52*), including RSC (*53*). Given that motor output encoding was greater than chance before trial onset (Fig. 5C, middle), we suspected that RSC neurons might encode bias from trial history and task variables from the current trial. To investigate this, we applied the same approach toward decoding the context, motor output, and trial outcome in the previous trial based on the responses of the current trial. We found that previous-trial context could not be decoded reliably during any epoch of the current trial (fig. S9, A to C). However, the previous-trial motor output could be decoded with high performance in the pretrial epoch (−1.5 to 0 s) and with low performance during the predecision epoch (0 to 3 s), but could not be decoded during the postdecision epoch (3 to 6 s; fig. S9, A to C). Last, previous-trial outcome could be decoded at high performance in the pretrial and early predecision epochs but not later in the trial (fig. S9, A to C). Previous trial type did have an effect on the following trial (fig. S9D), although the influence was suboptimal in terms of behavioral performance, with mice tending to repeat the previous motor selection. Together, this suggests that recent motor output and trial outcome are encoded in RSC activity (Fig. 5C, middle, and fig. S9), although note that trial history and motor bias on the upcoming trial are related and cannot be separated with this analysis.

Task variable encoding in RSC varies along the anterior-posterior axis

Dysgranular RSC extends several millimeters along the rostrocaudal axis in mice (*5*). To determine whether there are hemispheric or anatomical asymmetries in the encoding of task variables, we visualized the encoding performance of all task-responsive neurons organized by spatial position aligned to a reference atlas (Fig. 6A and movie S2; see Materials and Methods). Although encoding was similar across hemispheres (fig. S10), task variable encoding exhibited pronounced differences across posterior-to-anterior spatial positions (Fig. 6, B to F, and fig. S11). Encoding performance of the context was maximal in the posterior RSC population, weaker in the medial RSC, and virtually absent in the anterior RSC throughout the trial [Fig. 6, B (top row) to F]. On the other hand, although encoding performance during the pretrial period (context-independent motor bias) was high in the posterior RSC, as the trial progressed toward the decision point, task-driven increases in decoding performance were seen in the medial and anterior RSC, indicating a posterior-to-anterior flow of motor output encoding [Fig. 6, B (middle row) to F]. Last, high encoding performance of outcome immediately after the decision point was observed predominantly in the medial and anterior RSC, before becoming widespread shortly before the end of the trial [Fig. 6, B (bottom row) to F]. Results were qualitatively similar when RSC was divided into different numbers of regions (3 to 10 regions) and when cell number was homogenized across regions by sampling with replacement (fig. S11). Together, these results suggest anisotropy along the anterior-posterior axis in the encoding of task variables (Fig. 6G).

To determine whether this difference in encoding might be due to anatomical differences in cortical inputs and outputs, we performed anterograde and retrograde viral tracer experiments. First, we injected adeno-associated virus (AAV)–expressing green fluorescent protein in excitatory neurons of the visual cortex [areas posteromedial (PM) and anteromedial (AM), which project to RSC] (*54*) for anterograde labeling of visual cortical axon terminals in RSC (Fig. 7A). In the same mice, we injected retrograde-transported AAV (*55*) expressing red fluorescent protein into the CFA to label RSC neurons projecting to CFA (*35*, *36*), the primary cortical region active during planning and executing forelimb movements in our task (Fig. 7A). Both in vivo imaging and histology confirmed that visual cortical

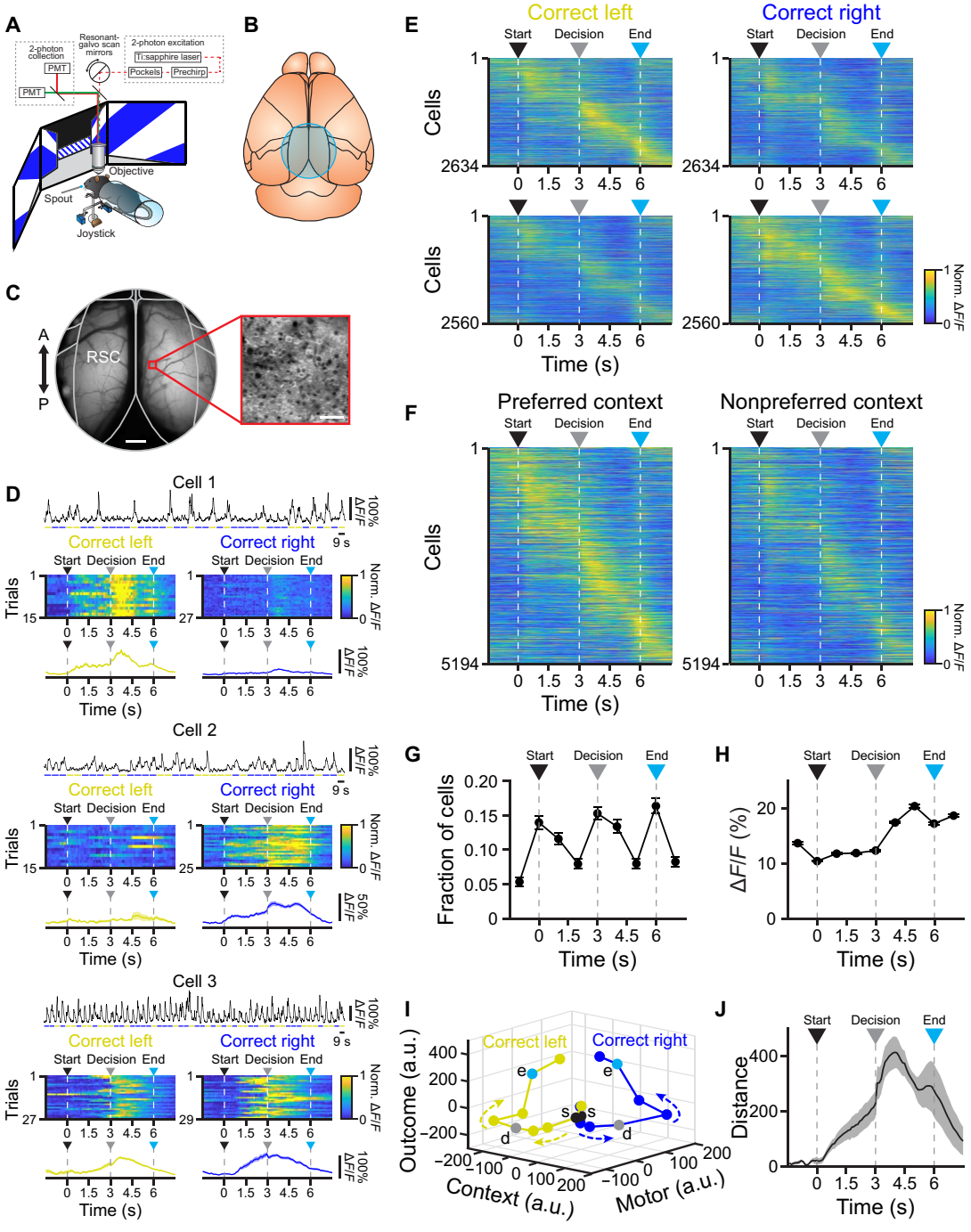

Fig. 4. Populations of RSC neurons exhibit selective responses spanning trial duration. (**A** and **B**) Imaging of excitatory neuron populations using two-photon microscopy (A) through a cranial window over bilateral RSC (B) during task performance. (**C**) Example 4-mm cranial window (left; scale bar, 500 μm) and two-photon imaging field (right); scale bar, 50 μm. (**D**) Example cells exhibiting selective responses for particular contexts (cells 1 to 2) or for both contexts with different dynamics (cell 3). For each cell: top: Δ*F*/*F* trace across concatenated correct trials for (context 1, yellow; context 2, blue). Middle: normalized responses across correct trials for context 1 (left) and context 2 (right). Bottom: average activity across correct context 1 (left) and context 2 (right) trials. (**E**) Average normalized activity of all neurons ($n = 10$ mice) preferring correct trials in context 1 (top, $n = 2634$ neurons) and context 2 (bottom, $n = 2560$ neurons). Averages include only even trials, sorted by peak latency on odd trials. (**F**) Average normalized activity for all responsive neurons ($n = 5194$ neurons from 10 mice) for the preferred (left) and nonpreferred (right) context. Averages include only even trials, sorted by peak latency on odd trials. (**G**) Fraction of neurons with peak activity at each trial time (mean ± 97.5% CIs). (**H**) Average peak response magnitude of all neurons as a function of trial time (mean ± SEM). (**I**) Neuronal activity trajectories for correct trials in both contexts obtained by targeted dimensionality reduction. Trajectories are initially similar but diverge as a result of the context and motor decision, followed by parallel displacement in the outcome dimension for both trajectories (s, trial start; d, decision point; e, trial end). a.u., arbitrary units. (**J**) Distance between trajectories described by neuronal activity in correct trials for both contexts (mean ± bootstrap-estimated SEM). Arrowheads indicate trial start (black), decision point (gray), and trial end (cyan).

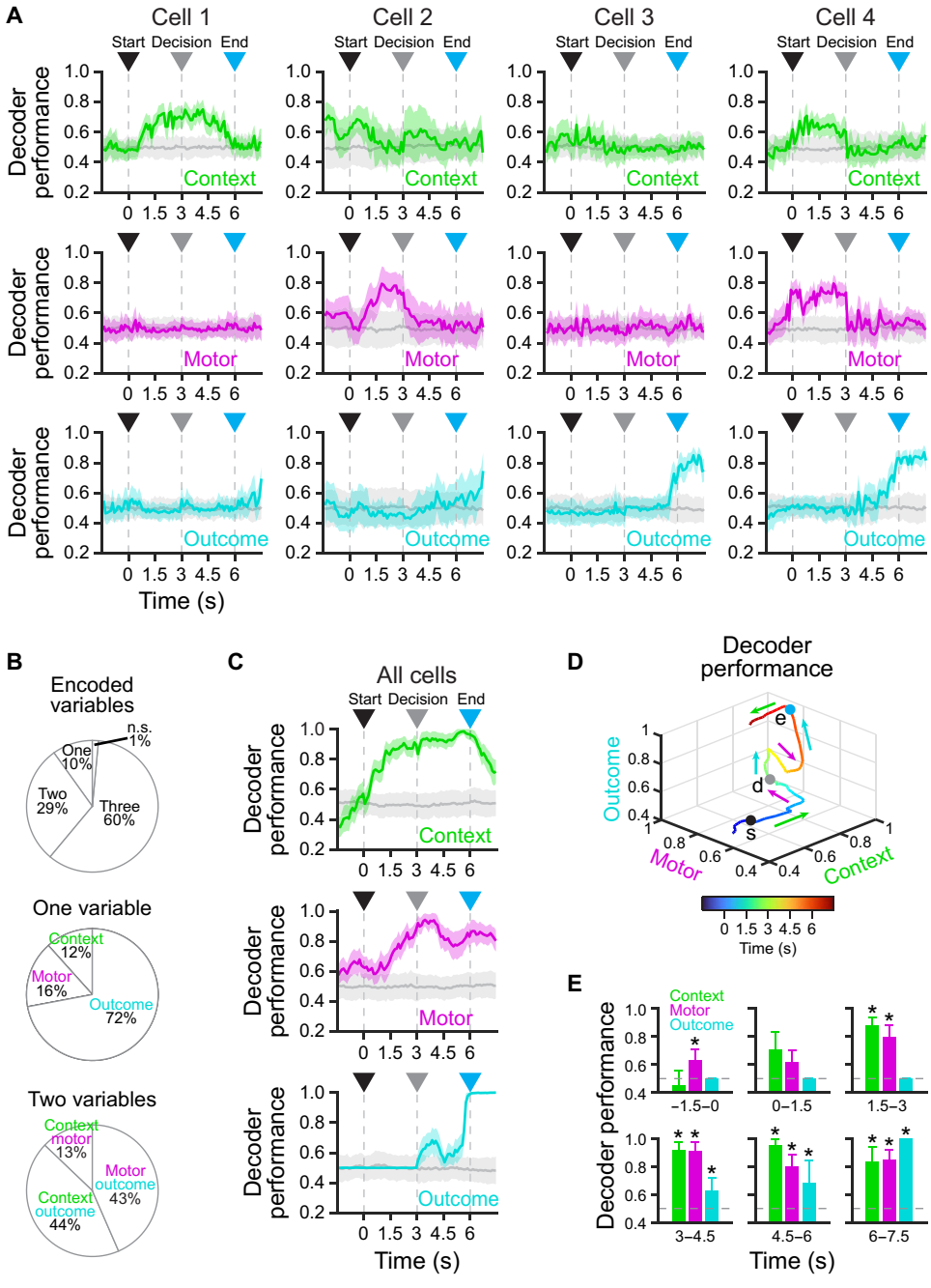

Fig. 5. RSC neurons encode task variables during context-trajectory associations. (**A**) Example cells exhibiting significant decoding of a single task variable (cell 1, context; cell 2, motor; cell 3, outcome) or multiple task variables (cell 4) using a support vector machine decoder (chance = 0.5; mean ± bootstrap-estimated SEM). (**B**) Top: proportion of cells ($n = 5194$ from 10 mice) significantly encoding one, two, three, or no task variables (see Materials and Methods). Middle: cells encoding a single task variable. Bottom: cells encoding a combination of two task variables. (**C**) Decoding of context (top), motor (middle), or outcome (bottom) by the entire population of recorded cells ($n = 5194$ from 10 mice) combined across sessions using a support vector machine classifier (chance = 0.5; mean ± bootstrap-estimated SEM). (**D**) Average trajectory described by population encoding of context, motor, and outcome mapped to each axis (s, trial start; d, decision point; e, trial end). Note that encoding of context precedes encoding of the eventual motor action, followed by encoding of outcome. (**E**) Bar plots showing significant encoding of the different task variables in different epochs ($n = 5194$ neurons from 10 mice; lower 5% CI > 0.5; mean ± bootstrap-estimated SEM). Arrowheads indicate trial start (black), decision point (gray), and trial end (cyan).

inputs predominantly targeted posterior RSC regions, consistent with previous findings (Fig. 7, B to D) (*56*, *57*). Conversely, RSC neurons projecting to CFA were located almost exclusively in anterior RSC (Fig. 7, B to D).

To further delineate the posterior-to-anterior RSC circuit, we performed additional retrograde and anterograde tracing experiments in posterior and anterior RSC (fig. S12). Major inputs to posterior RSC include medial visual cortices, presubiculum/subiculum,

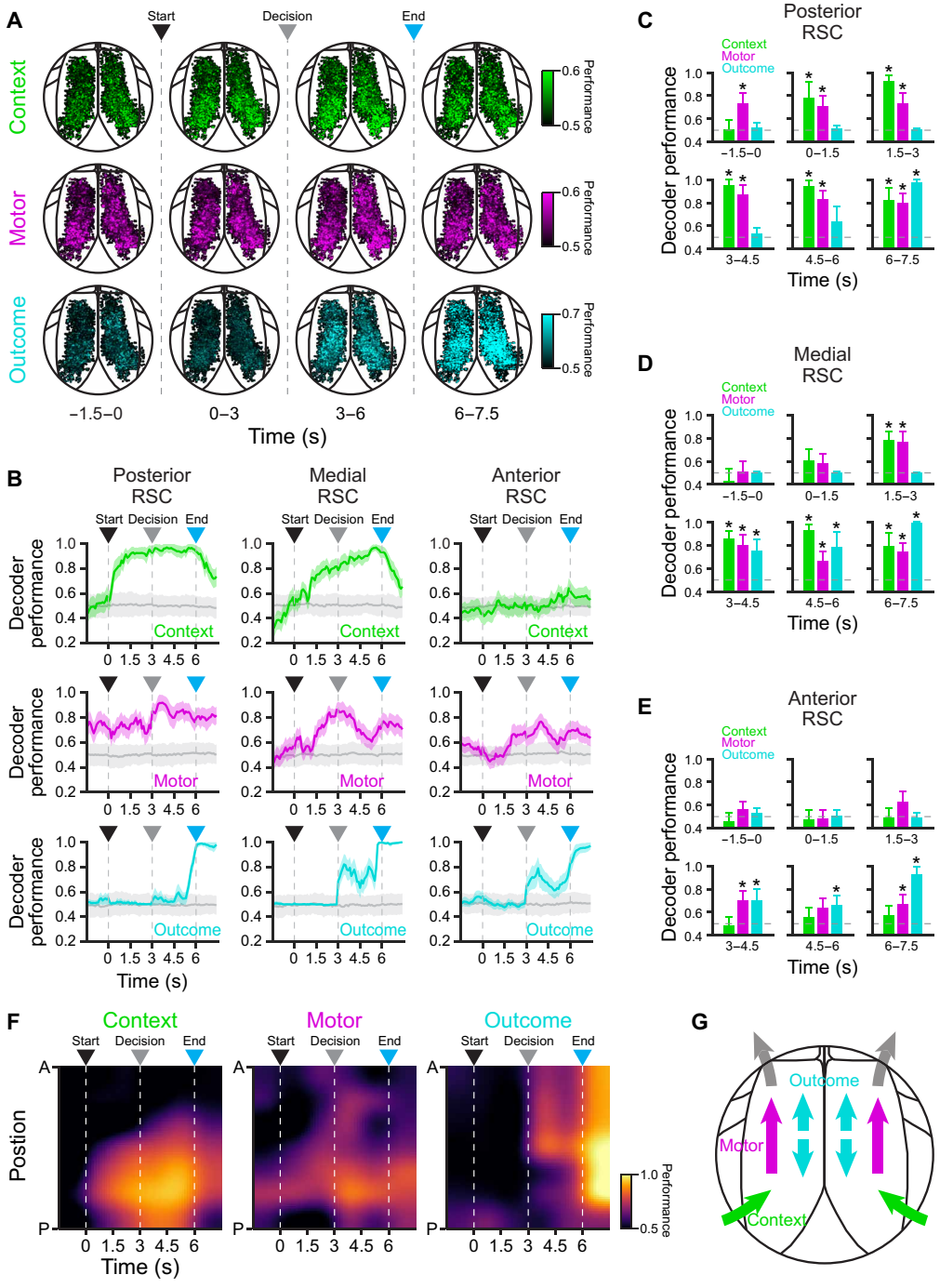

Fig. 6. Encoding of task variables varies along the anterior-posterior axis of RSC. (**A**) Maps displaying the contribution of individual RSC neurons to the encoding of context, motor, and outcome variables across different epochs throughout the trial using a support vector machine classifier ($n = 5194$ from 10 mice). Some cells are saturated to display dynamic range. (**B**) Encoding of context (top row), motor (middle row), and outcome (bottom row) by populations of neurons in posterior ($n = 1726$ neurons), medial ($n = 2493$ neurons), and anterior ($n = 975$ neurons) RSC (mean ± bootstrap-estimated SEM; shuffled trials in gray). Note that context is preferentially encoded in posterior RSC, whereas motor and outcome decoding are distributed across RSC with differing spatial and temporal dynamics. (**C** to **E**) Bar plots showing significant decoding in posterior (C; $n = 1726$ neurons), medial (D; $n = 2493$ neurons), and anterior (E; $n = 975$ neurons) RSC of context, motor, and outcome in different task epochs (asterisks, lower 5% CI > 0.5; mean ± bootstrap-estimated SEM). (**F**) Spatiotemporal encoding maps of context, motor, and outcome variables by RSC neurons ($n = 5194$). Context is mainly encoded in posterior RSC, with higher performance after trial start. By contrast, motor encoding is increased before trial start, revealing pretrial bias in motor output. Moreover, motor decoding transitions from posterior-to-anterior RSC before the decision point. Outcome is encoded throughout RSC, with a sharp increase in performance close to the reward time. (**G**) Proposed circuit architecture. Environmental context information from visual cortex enters posterior RSC, which then triggers motor planning activity in anterior RSC, including neurons projecting to CFA, the motor region controlling forelimb motor planning and movement. Outcome information is distributed across all RSC. Arrowheads indicate trial start (black), decision point (gray), and trial end (cyan).

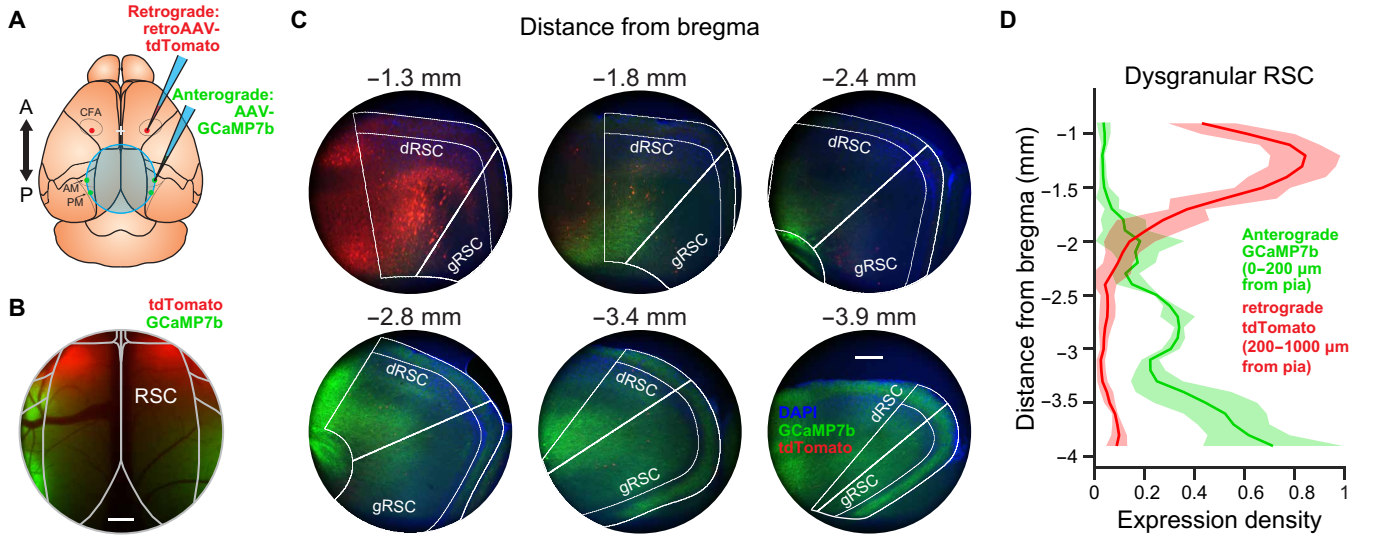

Fig. 7. An anatomical gradient of visual inputs and motor outputs in RSC. (**A**) Schematic of viral tracing experiments. An anterograde tracer (AAV.Syn.flex.GCaMP7b) was injected bilaterally into regions PM and AM of visual cortex in Emx1-Cre mice to achieve expression in excitatory projections neurons from visual cortex to RSC. A retrograde tracer (AAVrg.CAG.tdTomato) was injected bilaterally into CFA. Last, a cranial window was implanted over RSC for visualization under the widefield microscope. Cross indicates bregma. (**B**) Widefield image of RSC taken 21 days after virus injection. Scale bar, 500 μm. (**C**) Example coronal sections taken from anterior (−1.3 mm posterior to bregma) to posterior (−3.9 mm posterior to bregma) of RSC. Axonal expression of anterograde viral tracer (green) is present primarily in posterior RSC, while retrogradely labeled cell bodies (red) are almost exclusively located in anterior RSC. Nuclear stain [4′,6-diamidino-2-phenylindole (DAPI), blue] was used for structural visualization. Scale bar, 200 μm. (**D**) Normalized expression density (mean ± SD) for the anterograde tracer (visual cortical axons, green) in superficial layers (0 to 200 μm from pial surface) and the retrograde tracer (CFA-projecting cell bodies, red) in deep layers (200 to 1000 μm from pial surface) in dRSC. Distributions of expression density are significantly different ($n = 4$ hemispheres from two mice; $P = 0.0046$, Kolmogorov-Smirnov test).

the anterior thalamic nucleus, and the cingulate cortex (fig. S12, A, B, and G). Major inputs to anterior RSC include presubiculum, the superior colliculus, and posterior/medial RSC (fig. S12, C, D, and G). Major outputs of the anterior RSC include projections to motor and premotor cortices, PPC, cingulate cortex, and the dorsal striatum (fig. S12, E to G).

Together with the posterior-to-anterior asymmetry in spatiotemporal encoding of task variables (Fig. 6F), these results suggest a simple circuit architecture: Visual cues indicating the environmental context originating from visual cortex enter posterior RSC, polysynaptically triggering motor planning activity in anterior RSC, including in neurons projecting to CFA, the motor region controlling forelimb motor planning and movement (schematized in Fig. 6G).

DISCUSSION

Existing theories of RSC function during spatial navigation have posited that RSC is important for three interrelated functions: (i) direct encoding of egocentric and allocentric spatial variables (*3*–*5*), (ii) reference frame transformations between allocentric and egocentric representations (*2*, *3*, *5*, *58*), and (iii) encoding of the general environmental context independent of position (*4*–*7*). Although a number of recent studies have examined the encoding of spatial variables in RSC (*15*–*17*, *20*–*27*, *59*), much less is known about the role of RSC in encoding general context cues. Coding of environmental context is likely important both for modulating behavioral state and for guiding appropriate reference transformations during decisions. Here, we used a locomotion-independent context-to-trajectory association task to distinguish coding of the environmental context from local spatial variables, such as head direction or proximity to boundaries, which are correlated in freely moving or closed-loop behaviors. This approach revealed the distributed coding of environmental context, motor planning, and outcome in RSC during task performance.

Previous studies have indicated that RSC neurons exhibit weak responses to isolated visual stimuli, such as gratings or objects, even in the context of a behavioral task (*60*, *61*), although visual responses become more robust when they are useful for a spatial task (*24*). One reason for this may be that visual input to posterior RSC originates primarily from dorsal stream visual areas (*54*), which are specialized for the processing of coherent visual motion (*62*, *63*), and that RSC responses are particularly responsive to nasal-to-temporal movement (*57*). The RSC may thus be preferentially responsive to whole-field optic flow, textures, and other invariant spatial cues experienced during movement through space, as opposed to playing a general role in visual behaviors. In our study, we used abstract patterns for visual cues instead of unilateral cues presented on the side of the correct turn direction, as are typically used in virtual T-maze tasks (*45*, *64*, *65*). We reason that while RSC plays an important role for associating abstract features and contexts with appropriate motor responses, detection and orienting responses to unilateral cues rely more on subcortical structures such as the basal ganglia and superior colliculus (*66*–*69*).

Although our study focused on RSC, evidence suggests a range of other interconnected regions that also play a role in context-based navigational decisions. Although we see motor planning signals in RSC before movement execution (Fig. 5), similar signals have also been observed in posterior parietal cortex (*45*, *64*, *70*), secondary motor cortex (*44*, *45*, *71*, *72*), and hippocampus (*73*). In a recent study investigating the necessity of distributed cortical regions during

virtual navigation, only visual cortex was required for an orienting task (turning toward a cue), but a distributed network of VC, PPC, RSC, and motor cortex was required for tasks requiring accumulation or short-term memory of visual cues (*45*). The coordination of RSC activity with hippocampus, parietal cortex, and motor cortices during navigation requires further study. Future experiments using pathway-specific optogenetic suppression would be a powerful way to approach these questions. It will also be important to further dissect the intraregional RSC circuit, in particular, what information is carried by posterior-to-anterior RSC projections and whether silencing of these projections is sufficient to impair the association of context with motor action.

One important finding from our study is the distinct spatiotemporal dynamics of activity representing environmental context and motor planning in RSC. In particular, while posterior RSC encodes context and motor bias resulting from trial history, encoding of motor planning signals moved to medial and anterior RSC prior to the decision (Fig. 6 and fig. S11). These results are consistent with increased posterior-to-anterior flow of widefield calcium responses on correct trials in comparison to incorrect trials (fig. S3C), although some motor encoding can be found throughout the RSC (including medial RSC, which does not project to CFA). They are also consistent with anatomical data showing that inputs from visual cortex target posterior RSC (Fig. 7, B to D) (*56*, *57*), while outputs to motor cortex originate from anterior RSC (Fig. 7, B to D) (*74*). The anatomical differentiation was even more distinct, indicating that the neurons in posterior RSC encoding the visual context do not directly project to CFA but must instead influence motor planning signals in CFA through a polysynaptic pathway. Past work has shown that lesions to posterior RSC preferentially perturb visually guided spatial navigation, while lesions to anterior RSC disrupts internally guided navigation (*11*, *13*), further suggesting a functional asymmetry across the posterior-anterior axis. In concordance with this finding, human studies have noted a posterior-to-anterior gradient in RSC, with higher activity in posterior RSC during scene perception and higher activity in anterior RSC during episodic recall and self-referential processing (*75*, *76*). Given the necessity of RSC for the association of environmental context with motor choice and the anatomical differentiation we observed, our results suggest that context is converted into motor commands along the posterior-to-anterior axis of RSC, although we cannot rule out the possibility of cortico-cortico or cortico-striatal projections from posterior RSC influencing motor behavior indirectly. Future studies testing the importance of specific RSC inputs and outputs, as well as projections from posterior-to-anterior RSC, will be necessary to further dissect this circuit.

MATERIALS AND METHODS

Animals

To achieve widespread calcium indicator expression across dorsal cortex, we bred Emx1-Cre (Jax stock no. 005628) × ROSA-LNL-tTA (Jax stock no. 011008) × TITL-GCaMP6s (Jax stock no. 024104) triple transgenic mice (*77*) to express GCaMP6s in cortical excitatory neurons. For widefield ($n = 4$), photoinhibition ($n = 6$), two-photon imaging ($n = 10$), and anatomical tracer ($n = 2$) experiments, 12- to 16-week-old mice of both sexes were implanted with a head plate and cranial window. All mice used for widefield or two-photon imaging were checked for aberrant cortical activity (*78*), and no ictal events were identified in any of the mice. Water restriction started 7 days after recovery from surgical procedures, and behavioral training started after 7 days of water restriction (14 days after surgery). The animals were housed on a 12-hour light/12-hour dark cycle in cages of up to five animals before the implants and individually after the implants. All animal procedures were approved by the Institutional Animal Care and Use Committee at the University of California, Santa Barbara.

Surgical procedures

All surgeries were conducted under isoflurane anesthesia (3.5% induction and 1.5 to 2.5% maintenance). Before incision, the scalp was infiltrated with lidocaine (5 mg kg^{-1}, subcutaneous) for analgesia, and meloxicam (1 mg kg^{-1}, subcutaneous) was administered preoperatively to reduce inflammation. Once anesthetized, the scalp overlying the dorsal skull was sanitized and removed, and the periosteum was removed with a scalpel. For widefield imaging experiments, the skull was polished with conical rubber polishing bit, coated with cyanoacrylate (Loctite 406), and overlaid with an 8- to 10-mm round coverglass. For two-photon and photoinhibition experiments, the skull was abraded with a drill burr to improve adhesion of dental acrylic. Then, a 4- to 5-mm diameter craniotomy was made over the midline (centered at 2.5 to 3.0 mm posterior to bregma), leaving the dura intact. A cranial window was implanted over the craniotomy and sealed first with silicon elastomer (Kwik-Sil, World Precision Instruments) and then with dental acrylic (C&B-Metabond, Parkell) mixed with black ink to reduce light transmission. The cranial windows were made of two rounded pieces of coverglass (Warner Instruments) bonded with an ultraviolet-cured optical adhesive (Norland, NOA61). The bottom coverglass (4 mm) fit tightly inside the craniotomy, while the top coverglass (5 mm) was bonded to the skull using dental acrylic. A custom-designed stainless steel head plate (eMachineShop.com) was then affixed using dental acrylic. After surgery, mice were administered carprofen (5 to 10 mg kg^{-1}, oral) every 24 hours for 3 days to reduce inflammation.

Virtual T-maze design

Mice were head-fixed using custom restraint hardware (https://goard.mcdb.ucsb.edu/resources) and placed in polypropylene tubes to limit movement. A custom rotatory joystick, located within reach of mouse forelimbs, was mounted on optical hardware (Thorlabs) and attached to an optical encoder (Digi-key Electronics). Two servomotors (Adafruit Industries) were used to constrict the position of the joystick throughout the trial, allowing movement only during the decision window. The servos could also be opened unilaterally to allow turning responses in only one direction. A spout was placed near to the mouth of the mouse for delivery of water rewards (10 to 12 μl), which were controlled by a solenoid valve (Parker Hannifin). Licks were detected through a capacitive touch sensor connected to the metallic spout and to a metallic mesh inside the polypropylene tube. A virtual T-maze was displayed across three screens arranged in an arc to subtend 180° of the mouse visual field. All electronic components were controlled by custom code written in MATLAB (MathWorks) through Arduino Uno (Arduino). Computer-assisted design renderings were made in Fusion 360 (Autodesk).

Virtual mazes were built using the ViRMEn package (*79*), with modifications to control progression through the maze. We created two different virtual T-mazes with unique wall patterns, one consisting of horizontal yellow dashes on a black background (context 1; mean luminance, 10.6 ± 0.5 lux; mean ± SD; root mean square

contrast, 0.496) and one with oblique blue stripes on a white background (context 2; mean luminance: 13.4 ± 1.0 lux, mean ± SD; root mean square contrast: 0.414). The mazes were presented in pseudorandom order across an experimental session. Progression through virtual environment proceeded at a fixed speed throughout the trial, such that both traversal from the maze start to the decision point and traversal from the decision point to the end of the maze lasted 3 s each. During the decision window, two servomotors opened to allow rotation of the joystick with the forelimbs. All mice used both forelimbs to rotate the joystick. Rotation of the joystick was coupled to rotation of the field of view in the virtual environment. If the field-of-view rotation exceeded 45° to the left or to the right from the central position, a decision was registered, and the joystick was returned to the central position using the servomotors. If a decision was registered, then a tone was played, indicating the trial outcome (correct: 5 kHz, 70 dB tone for 0.25 s; incorrect: broadband white noise, 80 dB for 0.25 s), and the mouse was automatically rotated 90° in the chosen direction and then progressed to the end of the selected T-maze arm. The end of the rewarded arm contained a reward cue (a blue sphere) that was reached at the same time as water was administered, whereas the unrewarded arm did not contain the reward cue. As the mouse reached the end of the maze, the outcome tone was played again at the same frequency and volume but with longer duration (correct: 5 kHz, 70 dB tone for 1 s; incorrect: broadband white noise, 80 dB for 2 s). If no decision was detected within 3 s, then the joystick was returned to the center position using the servos, and the trial was aborted and not included in later analyses. At the end of each trial, there was a 3-s interval with a uniform blue (correct trial) or black (incorrect trial) screen before teleporting back to the start of the T-maze for the next trial. To avoid repeated presentations of the same maze, the probability for consecutively displaying the same context progressively decreased after a particular context was displayed, from 50 to 0% over 10 trials. To prevent bias, if the number responses to the left or to the right exceeded double the number of responses in the nonpreferred direction over a 10-trial window, then the context rewarded for the nonpreferred direction was consecutively displayed until bias was reduced below threshold.

In the closed loop version of the task, mice were allowed to rotate the field of view throughout the approach corridor with a maximum 50° rotation in either direction from the axis of traversal. Forward movement automatically progressed at a fixed speed. Decisions were registered if rotation exceeded 45° to the left or to the right once the mouse reached the decision point, otherwise optical flow stopped for a maximum of 3 s and resumed if a decision was detected.

Behavioral training

Before training, mice were gradually water restricted beginning 7 days after surgery. HydroGel (99% H_2O, ClearH20) was provided in decreasing amounts each day for 7 days (2.0 to 1.2 g). During training, mice were supplemented with HydroGel depending on the amount of water obtained in each particular session to keep their body weight at or above 85% of their initial weight, typically 1.2 ml of water (or HydroGel equivalent) per day. In addition, once per week (before nontraining days), mice received 2.0 g of HydroGel.

Starting 7 days after water restriction, mice spent 5 days of training on a habituation and shaping protocol. During this time, we unilaterally opened the servo to only allow correct decisions (forced choice trials). This stage was important for training mice to move the joystick in both directions without bias while also instructing them on the correct context-reward associations. Following shaping, the percentage of trials with free choices was progressively increased from 10 to 80%. Only free choices were used for all further analyses. Typically, it took mice 25 to 40 sessions to achieve plateau levels of performance. One mouse was removed from the study for health reasons before completion of training; all other mice were included.

For imaging sessions, in some cases, we acquired multiple sessions from the same field of neurons across subsequent days. Since decoding analyses require representation of all trial types (combinations of context and motor choice) and expert mice often make few incorrect choices, we selected imaging sessions a priori that contained the highest minimum number of each trial type, with a minimum of three trials of each trial type (correct trials, range = 8 to 56 trials, mean ± SD = 23.2 ± 9.7 trials; incorrect, range = 3 to 25 trials, mean ± SD = 7.8 ± 4.7 trials). Imaging sessions that failed this criterion for any of the four trial types were not included in further analyses. To ensure that our trial threshold did not affect our results, we repeated the analyses with minimum trial thresholds of four to seven trials. Although the neuron number decreased with more stringent thresholds, the spatiotemporal encoding profiles across task variables were similar.

Widefield imaging

For widefield imaging experiments (Fig. 2), GCaMP6s fluorescence was imaged through the skull (see the "Surgical procedures" section) using a custom widefield epifluorescence microscope (*63*) (https://goard.mcdb.ucsb.edu/resources). In brief, broad spectrum (400 to 700 nm) light-emitting diode (LED) illumination (Thorlabs, MNWHL4) was band-passed at 469 nm (Thorlabs, MF469-35) and reflected through a dichroic (Thorlabs, MD498) to the microscope objective (Olympus, MVPLAPO 2XC). Green fluorescence from the cortex passed through the dichroic and a bandpass filter (Thorlabs, MF525-39) to a scientific complementary metal-oxide semiconductor (PCO-Tech, pco.edge 4.2). Pixel frames (400 × 400) were acquired at 10 Hz with a field of view of 8.0 × 8.0 mm, leading to a pixel size of 0.02 mm pixel^{-1}. A custom light blocker (eMachineShop) affixed to the head plate was used to prevent light from the visual stimulus monitor from entering the imaging path. Measurement of hemodynamic signals was accomplished by illuminating with a green LED (550 nm, Prizmatix) every fourth frame to measure calcium-independent changes in fluorescence (*38*).

Widefield postprocessing

Images were acquired with camera control software (pco.edge) and saved into multipage TIF files. All subsequent image processing was performed in MATLAB (MathWorks). The $\Delta F/F$ for each individual pixel of each image frame was calculated as

$$\Delta F/F_{x,y,n} = \frac{(F_{x,y,n} - \widetilde{F}_{x,y})}{\widetilde{F}_{x,y}}$$

where $F_{x,y,n}$ is the fluorescence of pixel (x, y) at frame n, and $\widetilde{F}_{x,y}$ is defined as the median raw fluorescence value across the entire time series for pixel (x, y). Qualitatively similar results were obtained using a 30-s sliding window instead of the entire recording for determination of the $\widetilde{F}_{x,y}$. Subsequent analyses were performed on whole-frame $\Delta F/F$ matrices.

To define the borders of the different cortical regions for each mouse, we aligned the average projection of the dorsal cortex of each mouse to a template obtained from the Allen Mouse Brain Common

Coordinate Framework (*80*). In brief, we used custom software written in MATLAB (MathWorks) to scale and rotate the template into alignment using the superior sagittal sinus, the transverse sinus, and the borders of the dorsal cortex as reference points.

Space-frequency singular value decomposition was performed using Chronux 2.11 (http://chronux.org). In brief, average $\Delta F/F$ time series per mouse corresponding to each pixel were concatenated for correct and incorrect trials, respectively. Slepian sequences were then obtained using 10 tapers (time-bandwidth product = 10), and space-frequency singular value decomposition was calculated for projected pixel time series into frequencies between 0 and 5 Hz. The resulting decomposed time series represent orthogonal sets of spatial modes. The first mode was used as it explained the highest variability in our data (correct trials = 48.02% and incorrect trials = 40.89%). Gradients in the phase of decomposed time series indicate the direction of traveling waves in dorsal cortex during traversal of the virtual T-maze (*37*).

Photoinhibition experiments

Before cranial window implantation (see the "Surgical procedures" section), a series of 6 to 10 microinjections (50 to 100 nl each, 200- to 300-μm depth) of AAV5.Flex.ArchT.tdTomato (Addgene, #28305-AAV5) were delivered along the posterior-to-anterior axis of RSC (2.0 to 4.0 mm posterior, 0.5 mm lateral to bregma) in each hemisphere in triple transgenic GCaMP6s mice. Use of the Emx1-Cre line restricted viral expression of ArchT to excitatory RSC neurons. To characterize cortical inhibition, we performed widefield imaging during randomized periodic flashes (5 to 10 s) of 0.5 to 50 mW (0.04 to 4 mW m^{-2}) light, delivered to the cranial window with a fiber-coupled LED (550 nm, Prizmatix). The widefield $\Delta F/F$ immediately after (1 s) light offset was compared to widefield $\Delta F/F$ immediately before (1 s) onset. During optogenetic experiments in behaving mice, the RSC activity was suppressed by illumination with 40-mW (~3.2 mW mm^{-2}) 550-nm light from the maze onset until decision threshold was reached (3- to 6-s duration). A custom stainless-steel light blocker (eMachineShop.com) was mounted to the head plate to prevent LED light from the optogenetic stimulus from reaching the mouse eye. To control for heat-induced changes to neuronal activity or behavior (*41*), we used the same illumination parameters in a set of control mice expressing pan-excitatory GCaMP6s but not ArchT (light only controls).

Two-photon imaging

For two-photon imaging experiments, GCaMP6s fluorescence was imaged using a Prairie Investigator two-photon microscopy system with a resonant galvo scanning module (Bruker). Before two-photon imaging, widefield imaging was used to identify the RSC field by alignment to surface blood vessels.

For fluorescence excitation, we used a Ti:Sapphire laser (Mai-Tai eHP, Newport) with dispersion compensation (Deep See, Newport) tuned to λ = 920 nm. For collection, we used GaAsP photomultiplier tubes (Hamamatsu). To achieve a wide field of view, we used a 16×/0.8–numerical aperture microscope objective (Nikon) at an optical zoom of 2× (425 × 425 μm field). Imaging planes at a depth of 90 to 150 μm were imaged at a frame rate of 10 Hz. Laser power ranged from 40 to 75 mW at the sample depending on GCaMP6s expression levels. Photobleaching was minimal (<1% min^{-1}) for all laser powers used. A custom stainless-steel light blocker (eMachineShop) was mounted to the head plate and interlocked with a tube around the objective to prevent light from the visual stimulus monitor from reaching the photomultiplier tubes.

Two-photon postprocessing

Images were acquired using PrairieView acquisition software and converted into TIF files. All subsequent analyses were performed in MATLAB (MathWorks) using custom code (https://goard.mcdb.ucsb.edu/resources). First, images were corrected for *X*-*Y* movement by registration to a reference image (the pixel-wise mean of all frames) using two-dimensional cross-correlation.

To identify responsive neural somata, a pixel-wise activity map was calculated using a modified kurtosis measure. Neuron cell bodies were identified using local adaptive threshold and iterative segmentation. Automatically defined regions of interest (ROIs) were then manually checked for proper segmentation in a graphical user interface (allowing comparison to raw fluorescence and activity map images). To ensure that the response of individual neurons was not due to local neuropil contamination of somatic signals, a corrected fluorescence measure was estimated according to

$$F_{\text{corrected}}(n) = F_{\text{soma}}(n) - \alpha * (F_{\text{neuropil}}(n) - \overline{F_{\text{neuropil}}})$$

where F_{neuropil} was defined as the fluorescence in the region within 30 μm from the ROI border (excluding other ROIs) for frame n, $\overline{F_{\text{neuropil}}}$ is the average neuropil fluorescence across the entire time series, and α was chosen from [0 1] for each neuron to minimize the Pearson's correlation coefficient between $F_{\text{corrected}}$ and F_{neuropil}. The $\Delta F/F$ (%) for each neuron was then calculated as

$$\Delta F/F\,(\%) = 100 * (F_n - F_0)/F_0$$

Where F_n is the corrected fluorescence ($F_{\text{corrected}}$) for frame n, and F_0 is defined as the mode of the corrected fluorescence density distribution across the entire time series.

Analysis of two-photon imaging data

To determine whether a neuron exhibited consistent task-related activity, we calculated the Pearson's correlation coefficient between odd and even correct trials and compared it to the correlation coefficient of trials in which activity was circularly permuted a random sample number on each trial (time shuffled). If the original correlation coefficient was greater than the 97.5th percentile of the correlation coefficients from the time shuffled activity (1000 iterations), then the neuron was considered to exhibit reliable task-related activity and used for all subsequent analyses.

Targeted dimensionality reduction (Fig. 4) was performed as previously described (*42*, *44*). First, neuronal activity was denoised using the first 50 principal components analysis (explained variance = 62.09%). We then used linear regression on the principal components to define demixed task-related axes for context, motor choice, and outcome. Population trajectories were plotted for correct and incorrect trials in context 1 and context 2 as a function of time throughout the trial. Distances across trajectories were calculated as Euclidean distances in the reduced space for each time bin.

Encoding of task variables (*44*, *47*) was determined by support vector machine classifiers (*47*, *48*). To achieve this, trials were homogenized by sampling equal number of each trial type with replacement (correct left, incorrect right, incorrect left, and correct right) and then split into two nonoverlapping groups containing 50% of each trial type. This process ensures that all conditions comprise the same number of trials. Then, a support vector machine classifier was trained using 50% of trials and tested on the remaining

50% of trials per time bin. The performance SEM was obtained by taking the SD of bootstrapped samples (100 iterations). Encoding of the different variables was determined by comparing conditions as follows: (i) context, correct left and incorrect right versus incorrect left and correct right; (ii) motor, correct left and incorrect left versus incorrect right and correct right; and (iii) outcome, correct left and correct right versus incorrect right and incorrect left. A cell was considered to encode any of the task variables if the performance of the decoder was significantly higher than chance (0.5) for at least 5 consecutive bins (Wilcoxon sign-rank test).

Anatomical tracing

For anterograde tracing, we injected 100 µl of AAV1.Syn.Flex.GCaMP7b (Addgene, #104493-AAV1) bilaterally into visual area PM (−3.3 mm posterior, 1.6 mm lateral to bregma) and AM (−2.2 mm posterior, 1.7 mm lateral to bregma) or anterior RSC (−1.3 mm posterior, 0.5 mm lateral to bregma) of Slc17a7-Cre mice (Jax stock no. 023527) to express a green indicator in excitatory projection axons originating in visual cortex. For retrograde tracing, we made two 100-µl injections of AAVrg.CAG.tdTomato (Addgene, #59462-AAVrg) bilaterally into CFA (0.0 mm posterior, 1.6 to 2.0 mm lateral to bregma), posterior RSC (−3.9 mm posterior, 0.5 mm lateral to bregma), or anterior RSC (−1.3 mm posterior, 0.5 mm lateral to bregma). We then made a window centered over RSC as described previously. After 2 to 3 weeks, we performed widefield imaging, and then the animals were perfused with 4% paraformaldehyde. The brain was removed and placed in 4% PFA for 24 hours, followed by 24 hours in phosphate-buffered saline. We then cut 100-µm coronal slices and mounted them on slides with 4′,6-diamidino-2-phenylindole (Vector Laboratories, #H-1500-10). The slices were imaged on an Olympus BX51 fluorescence microscope and analyzed with MATLAB (MathWorks).

Statistical information

All data groups were compared using nonparametric tests (Wilcoxon rank sum, Wilcoxon signed-rank tests, or Kolmogorov-Smirnov test). Nested data were compared using a linear mixed-effects model with restricted maximum likelihood. Bootstrap estimates of SEM were calculated as the SD of values evaluated in 100 to 1000 shuffled iterations, obtained by randomly sampling with replacement from the original values. Differences were considered significant if they were outside the 95th percentile of the bootstrapped distribution.

SUPPLEMENTARY MATERIALS

Supplementary material for this article is available at http://advances.sciencemag.org/cgi/content/full/7/35/eabf9815/DC1

View/request a protocol for this paper from *Bio-protocol*.

REFERENCES AND NOTES

1. J. O'Keefe, J. Dostrovsky, The hippocampus as a spatial map. Preliminary evidence from unit activity in the freely-moving rat. *Brain Res.* **34**, 171–175 (1971).
2. N. Burgess, S. Becker, J. A. King, J. O'Keefe, Memory for events and their spatial context: Models and experiments. *Philos. Trans. R. Soc. B Biol. Sci.* **356**, 1493–1503 (2001).
3. S. D. Vann, J. P. Aggleton, E. A. Maguire, What does the retrosplenial cortex do? *Nat. Rev. Neurosci.* **10**, 792–802 (2009).
4. A. P. Miller, L. C. Vedder, M. L. Law, D. M. Smith, Cues, context, and long-term memory: The role of the retrosplenial cortex in spatial cognition. *Front. Hum. Neurosci.* **8**, (2014).
5. A. S. Mitchell, R. Czajkowski, N. Zhang, K. Jeffery, A. J. D. Nelson, Retrosplenial cortex and its role in spatial cognition. *Brain Neurosci. Adv.* **2**, 239821281875709 (2018).
6. D. M. Smith, A. M. P. Miller, L. C. Vedder, The retrosplenial cortical role in encoding behaviorally significant cues. *Behav. Neurosci.* **132**, 356–365 (2018).
7. T. P. Todd, D. I. Fournier, D. J. Bucci, Retrosplenial cortex and its role in cue-specific learning and memory. *Neurosci. Biobehav. Rev.* **107**, 713–728 (2019).
8. E. Teng, L. R. Squire, Memory for places learned long ago is intact after hippocampal damage. *Nature* **400**, 675–677 (1999).
9. G. K. Aguirre, M. D'Esposito, Topographical disorientation: A synthesis and taxonomy. *Brain* **122**, 1613–1628 (1999).
10. I. Q. Whishaw, H. Maaswinkel, C. L. Gonzalez, B. Kolb, Deficits in allothetic and idiothetic spatial behavior in rats with posterior cingulate cortex lesions. *Behav. Brain Res.* **118**, 67–76 (2001).
11. S. D. Vann, L. A. K. Wilton, J. L. Muir, J. P. Aggleton, Testing the importance of the caudal retrosplenial cortex for spatial memory in rats. *Behav. Brain Res.* **140**, 107–118 (2003).
12. S. D. Vann, J. P. Aggleton, Testing the importance of the retrosplenial guidance system: Effects of different sized retrosplenial cortex lesions on heading direction and spatial working memory. *Behav. Brain Res.* **155**, 97–108 (2004).
13. S. D. Vann, J. P. Aggleton, Selective dysgranular retrosplenial cortex lesions in rats disrupt allocentric performance of the radial-arm maze task. *Behav. Neurosci.* **119**, 1682–1686 (2005).
14. R. J. Sutherland, I. Q. Wishaw, B. Kolb, Contributions of cingulate cortex to two forms of spatial learning and memory. *J. Neurosci.* **8**, 1863–1872 (1988).
15. A. S. Alexander, D. A. Nitz, Retrosplenial cortex maps the conjunction of internal and external spaces. *Nat. Neurosci.* **18**, 1143–1151 (2015).
16. D. Mao, S. Kandler, B. L. McNaughton, V. Bonin, Sparse orthogonal population representation of spatial context in the retrosplenial cortex. *Nat. Commun.* **8**, 243 (2017).
17. D. Mao, A. R. Neumann, J. Sun, V. Bonin, M. H. Mohajerani, B. L. McNaughton, Hippocampus-dependent emergence of spatial sequence coding in retrosplenial cortex. *Proc. Natl. Acad. Sci. U.S.A.* **115**, 8015–8018 (2018).
18. L. L. Chen, L. H. Lin, E. J. Green, C. A. Barnes, B. L. McNaughton, Head-direction cells in the rat posterior cortex – I. Anatomical distribution and behavioral modulation. *Exp. Brain Res.* **101**, 8–23 (1994).
19. B. J. Clark, J. P. Bassett, S. S. Wang, J. S. Taube, Impaired head direction cell representation in the anterodorsal thalamus after lesions of the retrosplenial cortex. *J. Neurosci.* **30**, 5289–5302 (2010).
20. P. Y. Jacob, G. Casali, L. Spieser, H. Page, D. Overington, K. Jeffery, An independent, landmark-dominated head-direction signal in dysgranular retrosplenial cortex. *Nat. Neurosci.* **20**, 173–175 (2017).
21. L. C. Vedder, A. M. P. Miller, M. B. Harrison, D. M. Smith, Retrosplenial cortical neurons encode navigational cues, trajectories and reward locations during goal directed navigation. *Cereb. Cortex* **27**, 3713–3723 (2017).
22. A. S. Alexander, D. A. Nitz, Spatially periodic activation patterns of retrosplenial cortex encode route sub-spaces and distance traveled. *Curr. Biol.* **27**, 1551–1560.e4 (2017).
23. A. M. P. Miller, W. Mau, D. M. Smith, Retrosplenial cortical representations of space and future goal locations develop with learning. *Curr. Biol.* **29**, 2083–2090.e4 (2019).
24. L. F. Fischer, R. M. Soto-Albors, F. Buck, M. T. Harnett, Representation of visual landmarks in retrosplenial cortex. *eLife* **9**, e51458 (2020).
25. D. Mao, L. A. Molina, V. Bonin, B. L. McNaughton, Vision and locomotion combine to drive path integration sequences in mouse retrosplenial cortex. *Curr. Biol.* **30**, 1680–1688.e4 (2020).
26. A. S. Alexander, L. C. Carstensen, J. R. Hinman, F. Raudies, G. William Chapman, M. E. Hasselmo, Egocentric boundary vector tuning of the retrosplenial cortex. *Sci. Adv.* **6**, eaaz2322 (2020).
27. J. B. van Wijngaarden, S. S. Babl, H. T. Ito, Entorhinal-retrosplenial circuits for allocentric-egocentric transformation of boundary coding. *eLife* **9**, e59816 (2020).
28. T. Maviel, T. P. Durkin, F. Menzaghi, B. Bontempi, Sites of neocortical reorganization critical for remote spatial memory. *Science* **305**, 96–99 (2004).
29. R. Czajkowski, B. Jayaprakash, B. Wiltgen, T. Rogerson, M. C. Guzman-Karlsson, A. L. Barth, J. T. Trachtenberg, A. J. Silva, Encoding and storage of spatial information in the retrosplenial cortex. *Proc. Natl. Acad. Sci.* **111**, 8661–8666 (2014).
30. M. M. Milczarek, S. D. Vann, F. Sengpiel, Spatial memory engram in the mouse retrosplenial cortex. *Curr. Biol.* **28**, 1975–1980.e6 (2018).
31. K. A. Corcoran, M. D. Donnan, N. C. Tronson, Y. F. Guzmán, C. Gao, V. Jovasevic, A. L. Guedea, J. Radulovic, NMDA receptors in retrosplenial cortex are necessary for retrieval of recent and remote context fear memory. *J. Neurosci.* **31**, 11655–11659 (2011).
32. M. J. Buckley, A. S. Mitchell, Retrosplenial cortical contributions to anterograde and retrograde memory in the monkey. *Cereb. Cortex* **26**, 2905–2918 (2016).
33. K. K. Cowansage, T. Shuman, B. C. Dillingham, A. Chang, P. Golshani, M. Mayford, Direct reactivation of a coherent neocortical memory of context. *Neuron* **84**, 432–441 (2014).
34. A. F. De Sousa, K. K. Cowansage, I. Zutshi, L. M. Cardozo, E. J. Yoo, S. Leutgeb, M. Mayford, Optogenetic reactivation of memory ensembles in the retrosplenial cortex induces systems consolidation. *Proc. Natl. Acad. Sci. U.S.A.* **116**, 8576–8581 (2019).
35. K. Morandell, D. Huber, The role of forelimb motor cortex areas in goal directed action in mice. *Sci. Rep.* **7**, 15759 (2017).
36. K. A. Tennant, D. L. Adkins, N. A. Donlan, A. L. Asay, N. Thomas, J. A. Kleim, T. A. Jones, The organization of the forelimb representation of the C57BL/6 mouse motor cortex as defined by intracortical microstimulation and cytoarchitecture. *Cereb. Cortex* **21**, 865–876 (2011).

37. H. Makino, C. Ren, H. Liu, A. N. Kim, N. Kondapaneni, X. Liu, D. Kuzum, T. Komiyama, Transformation of cortex-wide emergent properties during motor learning. *Neuron* **94**, 880–890.e8 (2017).
38. J. B. Wekselblatt, E. D. Flister, D. M. Piscopo, C. M. Niell, Large-scale imaging of cortical dynamics during sensory perception and behavior. *J. Neurophysiol.* **115**, 2852–2866 (2016).
39. S. S. Babl, B. P. Rummell, T. Sigurdsson, The spatial extent of optogenetic silencing in transgenic mice expressing channelrhodopsin in inhibitory interneurons. *Cell Rep.* **29**, 1381–1395.e4 (2019).
40. T. M. Otchy, S. B. E. Wolff, J. Y. Rhee, C. Pehlevan, R. Kawai, A. Kempf, S. M. H. Gobes, B. P. Ölveczky, Acute off-target effects of neural circuit manipulations. *Nature* **528**, 358–363 (2015).
41. S. F. Owen, M. H. Liu, A. C. Kreitzer, Thermal constraints on in vivo optogenetic manipulations. *Nat. Neurosci.* **22**, 1061–1065 (2019).
42. V. Mante, D. Sussillo, K. V. Shenoy, W. T. Newsome, Context-dependent computation by recurrent dynamics in prefrontal cortex. *Nature* **503**, 78–84 (2013).
43. G. N. Pho, M. J. Goard, J. Woodson, B. Crawford, M. Sur, Task-dependent representations of stimulus and choice in mouse parietal cortex. *Nat. Commun.* **9**, 2596 (2018).
44. M. J. Goard, G. N. Pho, J. Woodson, M. Sur, Distinct roles of visual, parietal, and frontal motor cortices in memory-guided sensorimotor decisions. *eLife* **5**, e13764 (2016).
45. L. Pinto, K. Rajan, B. DePasquale, S. Y. Thiberge, D. W. Tank, C. D. Brody, Task-dependent changes in the large-scale dynamics and necessity of cortical regions. *Neuron* **104**, 810–824.e9 (2019).
46. L. Pinto, Y. Dan, Cell-type-specific activity in prefrontal cortex during goal-directed behavior. *Neuron* **87**, 437–450 (2015).
47. D. Raposo, M. T. Kaufman, A. K. Churchland, A category-free neural population supports evolving demands during decision-making. *Nat. Neurosci.* **17**, 1784–1792 (2014).
48. N. Shahidi, A. R. Andrei, M. Hu, V. Dragoi, High-order coordination of cortical spiking activity modulates perceptual accuracy. *Nat. Neurosci.* **22**, 1148–1158 (2019).
49. S. Musall, M. T. Kaufman, A. L. Juavinett, S. Gluf, A. K. Churchland, Single-trial neural dynamics are dominated by richly varied movements. *Nat. Neurosci.* **22**, 1677–1686 (2019).
50. C. Stringer, M. Pachitariu, N. Steinmetz, C. B. Reddy, M. Carandini, K. D. Harris, Spontaneous behaviors drive multidimensional, brainwide activity. *Science* **364**, 255 (2019).
51. E. J. Hwang, J. E. Dahlen, M. Mukundan, T. Komiyama, History-based action selection bias in posterior parietal cortex. *Nat. Commun.* **8**, 1242 (2017).
52. A. Akrami, C. D. Kopec, M. E. Diamond, C. D. Brody, Posterior parietal cortex represents sensory history and mediates its effects on behaviour. *Nature* **554**, 368–372 (2018).
53. R. Hattori, B. Danskin, Z. Babic, N. Mlynaryk, T. Komiyama, Area-specificity and plasticity of history-dependent value coding during learning. *Cell* **177**, 1858–1872.e15 (2019).
54. Q. Wang, O. Sporns, A. Burkhalter, Network analysis of corticocortical connections reveals ventral and dorsal processing streams in mouse visual cortex. *J. Neurosci.* **32**, 4386–4399 (2012).
55. D. G. R. Tervo, B.-Y. Hwang, S. Viswanathan, T. Gaj, M. Lavzin, K. D. Ritola, S. Lindo, S. Michael, E. Kuleshova, D. Ojala, C.-C. Huang, C. R. Gerfen, J. Schiller, J. T. Dudman, A. W. Hantman, L. L. Looger, D. V. Schaffer, A. Y. Karpova, A designer AAV variant permits efficient retrograde access to projection neurons. *Neuron* **92**, 372–382 (2016).
56. S. W. Oh, J. A. Harris, L. Ng, B. Winslow, N. Cain, S. Mihalas, Q. Wang, C. Lau, L. Kuan, A. M. Henry, M. T. Mortrud, B. Ouellette, T. N. Nguyen, S. A. Sorensen, C. R. Slaughterbeck, W. Wakeman, Y. Li, D. Feng, A. Ho, E. Nicholas, K. E. Hirokawa, P. Bohn, K. M. Joines, H. Peng, M. J. Hawrylycz, J. W. Phillips, J. G. Hohmann, P. Wohnoutka, C. R. Gerfen, C. Koch, A. Bernard, C. Dang, A. R. Jones, H. Zeng, A mesoscale connectome of the mouse brain. *Nature* **508**, 207–214 (2014).
57. A. Powell, W. M. Connelly, A. Vasalauskaite, A. J. D. Nelson, S. D. Vann, J. P. Aggleton, F. Sengpiel, A. Ranson, Stable encoding of visual cues in the mouse retrosplenial cortex. *Cereb. Cortex* **30**, 4424–4437 (2020).
58. A. Bicanski, N. Burgess, A neural-level model of spatial memory and imagery. *eLife* **7**, e33752 (2018).
59. J. Voigts, M. T. Harnett, Somatic and dendritic encoding of spatial variables in retrosplenial cortex differs during 2D navigation. *Neuron* **105**, 237–245.e4 (2020).
60. A. Harel, D. J. Kravitz, C. I. Baker, Deconstructing visual scenes in cortex: Gradients of object and spatial layout information. *Cereb. Cortex* **23**, 947–957 (2013).
61. N. A. Steinmetz, P. Zatka-Haas, M. Carandini, K. D. Harris, Distributed coding of choice, action and engagement across the mouse brain. *Nature* **576**, 266–273 (2019).
62. A. B. Saleem, Two stream hypothesis of visual processing for navigation in mouse. *Curr. Opin. Neurobiol.* **64**, 70–78 (2020).
63. K. K. Sit, M. J. Goard, Distributed and retinotopically asymmetric processing of coherent motion in mouse visual cortex. *Nat. Commun.* **11**, 3565 (2020).
64. C. D. Harvey, P. Coen, D. W. Tank, Choice-specific sequences in parietal cortex during a virtual-navigation decision task. *Nature* **484**, 62–68 (2012).
65. M. Krumin, J. J. Lee, K. D. Harris, M. Carandini, Decision and navigation in mouse parietal cortex. *eLife* **7**, e42583 (2018).
66. P. Znamenskiy, A. M. Zador, Corticostriatal neurons in auditory cortex drive decisions during auditory discrimination. *Nature* **497**, 482–485 (2013).
67. L. Wang, K. McAlonan, S. Goldstein, C. R. Gerfen, R. J. Krauzlis, A causal role for mouse superior colliculus in visual perceptual decision-making. *J. Neurosci.* **40**, 3768–3782 (2020).
68. M. M. Yartsev, T. D. Hanks, A. M. Yoon, C. D. Brody, Causal contribution and dynamical encoding in the striatum during evidence accumulation. *eLife* **7**, e34929 (2018).
69. R. Huda, M. J. Goard, G. N. Pho, M. Sur, Neural mechanisms of sensorimotor transformation and action selection. *Eur. J. Neurosci.* **49**, 1055–1060 (2019).
70. L. N. Driscoll, N. L. Pettit, M. Minderer, S. N. Chettih, C. D. Harvey, Dynamic reorganization of neuronal activity patterns in parietal cortex. *Cell* **170**, 986–999.e16 (2017).
71. J. C. Erlich, B. W. Brunton, C. A. Duan, T. D. Hanks, C. D. Brody, Distinct effects of prefrontal and parietal cortex inactivations on an accumulation of evidence task in the rat. *eLife* **4**, e05457 (2015).
72. J. M. Olson, J. K. Li, S. E. Montgomery, D. A. Nitz, Secondary motor cortex transforms spatial information into planned action during navigation. *Curr. Biol.* **30**, 1845–1854.e4 (2020).
73. R. A. Gulli, L. R. Duong, B. W. Corrigan, G. Doucet, S. Williams, S. Fusi, J. C. Martinez-Trujillo, Context-dependent representations of objects and space in the primate hippocampus during virtual navigation. *Nat. Neurosci.* **23**, 103–112 (2020).
74. N. Yamawaki, J. Radulovic, G. M. G. Shepherd, A corticocortical circuit directly links retrosplenial cortex to M2 in the mouse. *J. Neurosci.* **36**, 9365–9374 (2016).
75. E. H. Silson, A. W. Gilmore, S. E. Kalinowski, A. Steel, A. Kidder, A. Martin, C. I. Baker, A posterior–anterior distinction between scene perception and scene construction in human medial parietal cortex. *J. Neurosci.* **39**, 705–717 (2019).
76. E. R. Chrastil, Heterogeneity in human retrosplenial cortex: A review of function and connectivity. *Behav. Neurosci.* **132**, 317–338 (2018).
77. L. Madisen, A. R. Garner, D. Shimaoka, A. S. Chuong, N. C. Klapoetke, L. Li, A. van der Bourg, Y. Niino, L. Egolf, C. Monetti, H. Gu, M. Mills, A. Cheng, B. Tasic, T. N. Nguyen, S. M. Sunkin, A. Benucci, A. Nagy, A. Miyawaki, F. Helmchen, R. M. Empson, T. Knöpfel, E. S. Boyden, R. C. Reid, M. Carandini, H. Zeng, Transgenic mice for intersectional targeting of neural sensors and effectors with high specificity and performance. *Neuron* **85**, 942–958 (2015).
78. N. A. Steinmetz, C. Buetfering, J. Lecoq, C. R. Lee, A. J. Peters, E. A. K. Jacobs, P. Coen, D. R. Ollerenshaw, M. T. Valley, S. E. J. De Vries, M. Garrett, J. Zhuang, P. A. Groblewski, S. Manavi, J. Miles, C. White, E. Lee, F. Griffin, J. D. Larkin, K. Roll, S. Cross, T. V. Nguyen, R. Larsen, J. Pendergraft, T. Daigle, B. Tasic, C. L. Thompson, J. Waters, S. Olsen, D. J. Margolis, H. Zeng, M. Hausser, M. Carandini, K. D. Harris, Aberrant cortical activity in multiple GCaMP6-expressing transgenic mouse lines. *eNeuro* **4**, ENEURO.0207-17.2017 (2017).
79. D. Aronov, D. W. Tank, Engagement of neural circuits underlying 2D spatial navigation in a rodent virtual reality system. *Neuron* **84**, 442–456 (2014).
80. Q. Wang, S. L. Ding, Y. Li, J. Royall, D. Feng, P. Lesnar, N. Graddis, M. Naeemi, B. Facer, A. Ho, T. Dolbeare, B. Blanchard, N. Dee, W. Wakeman, K. E. Hirokawa, A. Szafer, S. M. Sunkin, S. W. Oh, A. Bernard, J. W. Phillips, M. Hawrylycz, C. Koch, H. Zeng, J. A. Harris, L. Ng, The Allen Mouse Brain Common Coordinate Framework: A 3D reference atlas. *Cell* **181**, 936–953.e20 (2020).

Acknowledgments: We thank D. A. Nitz, A. Banerjee, S. Kandler, and D. Mao for comments on the manuscript; T. Marks for assistance with histology experiments; and S. Gelfer, E. Hutchings, N. Glick, and A. Ortiz for assistance with behavioral training. **Funding:** This work was supported by the following: Harvey Karp Discovery Award (L.M.F.), UC MEXUS-CONACYT Postdoctoral Fellowship (L.M.F.), NIH R00MH104259 (M.J.G.), NSF 1707287 (M.J.G.), Hellman Fellows Fund (M.J.G.), Larry L. Hillblom Foundation (M.J.G.), and Whitehall Foundation (M.J.G.). **Author contributions:**, Conceptualization: L.M.F. and M.J.G. Methodology: L.M.F. and M.J.G. Investigation: L.M.F. Formal analysis: L.M.F. and M.J.G. Writing (original draft): L.M.F. and M.J.G. Writing (review and editing): L.M.F. and M.J.G. **Competing interests:** The authors declare that they have no competing interests. **Data and materials availability:** All data needed to evaluate the conclusions in the paper are present in the paper and the Supplementary Materials. Responses from individual neurons imaged by two-photon imaging and source data for behavioral and widefield experiments are available in the following repository: https://doi.org/10.25349/D99W4T. Correspondence and requests should be directed to michael.goard@lifesci.ucsb.edu.

Submitted 2 December 2020
Accepted 2 July 2021
Published 25 August 2021
10.1126/sciadv.abf9815

Citation: L. M. Franco, M. J. Goard, A distributed circuit for associating environmental context with motor choice in retrosplenial cortex. *Sci. Adv.* **7**, eabf9815 (2021).

ScienceAdvances

A distributed circuit for associating environmental context with motor choice in retrosplenial cortex

Luis M. FrancoMichael J. Goard

Sci. Adv., 7 (35), eabf9815. • DOI: 10.1126/sciadv.abf9815

Science Advances (ISSN) is published by the American Association for the Advancement of Science. 1200 New York Avenue NW, Washington, DC 20005. The title *Science Advances* is a registered trademark of AAAS.